

Ab initio simulation and thermodynamic analysis of the forsterite Mg_2SiO_4 (010) surface structure

Ming Geng^{1,2,*} and Hannes Jónsson^{3,4,†}

¹*Key Laboratory of Earth and Planetary Physics, Institute of Geology and Geophysics, Chinese Academy of Sciences, Beijing 100029, China*

²*Institutions of Earth Science, Chinese Academy of Sciences, China*

³*Faculty of Physical Sciences, University of Iceland, 107 Reykjavík, Iceland*

⁴*COMP Centre of Excellence and Department of Applied Physics, Aalto University, FIN-00076 Espoo, Finland*

(Dated: April 23, 2022)

The surface stability of possible termination structures for (010) of forsterite Mg_2SiO_4 was studied using a first-principles-based thermodynamic approach. The Density functional theory (DFT) calculation enables us to estimate the surface Gibbs free energy of different surface structures and compare the stability of different surfaces as functions of the chemical environment. We found that among nine possible terminations, the SiO-II, M2, O-II termination could be stable from the Mg-poor condition to the Mg-rich condition. This relative stability order remains in the high-temperature situation. The phase diagram obtained provides ground for further theoretical studies of chemical processes on the forsterite surface.

I. INTRODUCTION

Silicate minerals are the building blocks of terrestrial planets. In a wide variety of silicate minerals, olivine is a predominant mineral in both Earth's upper mantle and interstellar media in space. Olivines are silicate solid solutions with the general formula $(Mg_xFe_{2-x})SiO_4$ from the pure magnesium end member forsterite to the iron end member fayalite. However, both on Earth and in space, most common olivines are richer in magnesium than in iron. Crystal olivines present an orthorhombic structure with space group $Pbmn$ and are characterized to have $[SiO_4]^{4-}$ tetrahedra linked by the divalent metal cations as indicated in Fig.1. Consequently, olivine plays a fundamental role in defining the properties and influencing the physiochemical processes of the terrestrial planet interior. Knowledge of physical and chemical properties of olivine is of great geophysical and astrophysical interest because they are related to many important processes.

The exposed surface structure or termination of forsterite Mg_2SiO_4 is highly related to the adsorption ability to volatile elements, which is important in many natural processes. For example, the chemisorption of water molecules onto forsterite dust grain has been considered the possible source of water for terrestrial planets¹⁻⁴. Despite the low porosity and permeability, formations of ultramafic rock peridotite are potentially attractive sites for permanent carbon dioxide sequestration because of the high olivine content and thus significant potential for carbon dioxide mineralization⁵. Following the subduction of the tectonic plate, carbonated peridotite (Olivine + CO_2) and serpentinization (Olivine + H_2O) can transport carbon and water into the deep interior of the Earth. This process is the most essential pathway of the volatile element cycle of the Earth and affects many important features of our planet. Therefore, a fundamental understanding of the stability of the surface structure of

Mg_2SiO_4 under various reaction conditions must be developed.

A preliminary investigation of the relative stabilities of various crystalline surfaces is required to understand many surface-related phenomena. A comprehensive knowledge of the olivine surface energetics and morphology at the atomic level is of extreme importance to understanding the true nature of all processes that involve the olivine interface. Several computational studies based on the force-field calculation^{6,7} were performed on the main low-index surface of forsterite. Recently, ab initio calculations⁸⁻¹¹ with different basis sets have been done to reconfirm the main surface stability order. Both force-field and ab initio calculations yield similar results that the (010) surface is considered the most stable one among several low-index surfaces. With these results, many studies have moved forward to the absorption of volatile atoms and molecules, such as H atom¹⁰ and water molecule¹². All studies are based on non-polar surfaces, but for the adsorption study, both non-polar and polar surface terminations may be important. After a careful examine of previous studies, we have found that the surface termination in the adsorption researches are not identical because of the arbitrary selection of the researchers. A recent experimental work observed different surface terminations and their different hydrations of forsterite (010) with high-resolution X-ray reflectivity (HRXR)¹³ after different polishing methods were used in the sample preparation. Thus, termination differences should also be considered in evaluating the relative stability of a surface, particularly in adsorption studies.

In this article, we present simulations of Mg_2SiO_4 (010) surfaces with all possible terminations and analyse their structure and surface stabilities at various oxygen partial pressures and temperatures with a first-principles-based thermodynamic approach.

Section II describes the computational details of our calculations and surface structures. Section III contains the results obtained from the calculations of the elec-

tronic structures and thermodynamic stability of surfaces and further discussion. The conclusions are summarized in Section IV.

II. METHOD

A. Surface structures

There are 2 different metal ion sites, 3 oxygen sites and one silicon site in forsterite. In the [010] orientation of forsterite Mg_2SiO_4 , the atomic layers are stacked $2Mg(M1) - O(O1) - SiO(O3) - 2O(O2) - Mg(M2) - Mg(M2) - 2O(O2) - SiO(O3) - O(O1) - 2Mg(M1) -$. Crystal planes with [010] orientation can have 9 different surface terminations. In the present study, we construct nine slabs with these nine structurally different (010) surface terminations. We name the slabs after the cut positions of the atomic stack: M1 (metal site 1), SiO (O3 and Si site), O (O1 site), $O2$ (O2 site) and M2 (metal site 2). Because M1 (metal site 1) is on the symmetric line, it can have only one termination in the position. The other four cut sites (SiO , O , $O2$ and M2) can form two different surface structures in opposite directions. We use a "-II" mark to distinguish different slabs in the same position. We construct the same termination on both sides of every slab. In these nine slabs, only the M2 termination is stoichiometric.

B. Cleavage Energies

When we cleave a forsterite crystal, we can create two complementary surfaces. There are five complementary pairs of surfaces for the forsterite [010] orientation. The M2-terminated surface is complementary to itself, and the created slab is stoichiometric.

In the present study, we use asymmetric slabs terminated with different surfaces on two sides but maintain the stoichiometric slab as the unit bulk crystal. Since the combination of two slabs with complementary terminations is a two-time-thick unit bulk crystal, the cleavage energy is the energy required to cleave a crystal. Therefore, the cleavage energies per unit cell are calculated as follows

$$E_{cleave}(i, j) = -\frac{1}{2}[E_{slab}^i + E_{slab}^j - 2E_{Mg_2SiO_4}^{bulk}] \quad (1)$$

where $E_{Mg_2SiO_4}^{bulk}$ is the total energy for unit cell of Mg_2SiO_4 , and E_{slab}^i and E_{slab}^j are the total energies for complementary surface slabs. The cleavage energy density per unit area is equal to

$$\epsilon_{cleave}(i, j) = \frac{E_{cleave}(i, j)}{A} \quad (2)$$

where A is the surface unit cell area.

C. Computational details

We used the Vienna Ab-initio Simulation Package (VASP) code¹⁴⁻¹⁷ to perform the DFT calculations. The projector-augmented wave (PAW) method¹⁸ is used to describe the electron-ion potential. The Perdew-Burke-Ernzerhof (PBE) form exchange-correlation potential approximation¹⁹ is used with a 500 eV kinetic energy cut-off. The ground-state atomic geometries of the bulk and surface were obtained by minimizing the forces on each atom to below 0.01 eV/Å. Monkhorst-Pack k-point mesh schemes were used in the optimization for bulk phases ($8 \times 8 \times 8$) and surface terminations ($8 \times 8 \times 1$). To minimize the effect of the periodic boundary condition, we add a 30 Å-thick vacuum space on top of every surface slab model.

D. Thermodynamic stability

The thermodynamic formalism in our study estimates the stability of forsterite surfaces in equilibrium with O_2 and oxides. The internal energy only characterizes systems with a constant chemical composition. Gibbs free energies can account for the exchange of atoms between the bulk crystal, its surface and the gas phase into the analysis of the surface stability. The surface Gibbs free energy is a measure of excess energy of a semi-infinite crystal in contact with matter reservoirs with respect to the bulk crystal. The most stable surface has a structure with the smallest surface Gibbs free energy among all possible surface structures.

The surface Gibbs free energies are functions of chemical potentials of different atomic species. For example, the surface Gibbs free energy of the forsterite slab is:

$$\Omega_i = \frac{1}{2}(G_{slab}^i - N_{Mg}\mu_{Mg} - N_{Si}\mu_{Si} - N_O\mu_O) \quad (3)$$

where N_{Mg} , N_{Si} , N_O denote the numbers of Mg, Si and O atoms in the slab; G_{slab}^i is the Gibbs free energy of the symmetric slab with identical surface terminations on both top and bottom sides; and μ_{Mg} , μ_{Si} and μ_O are the chemical potentials for the Mg, Si and O atomic species in the forsterite crystal. The surface Gibbs free energy per unit area is

$$\omega = \frac{\Omega}{A} \quad (4)$$

Because the surface of each slab is in equilibrium with bulk forsterite, the chemical potential of Mg_2SiO_4 is equal to the bulk crystal Gibbs free energy, which results in the following expression:

$$\mu_{Mg_2SiO_4} = g_{Mg_2SiO_4}^{bulk} \quad (5)$$

$\mu_{Mg_2SiO_4}$ is the chemical potential of forsterite, which is equal to the sum of the chemical potentials of all atom types in the Mg_2SiO_4 crystal:

$$\mu_{Mg_2SiO_4} = 2\mu_{Mg} + \mu_{Si} + 4\mu_O \quad (6)$$

We follow a method of previous studies of different chemical systems to simplify the equation for the surface Gibbs free energy as a function of the variations of the Mg chemical potential and O chemical potential.

$$\Omega^i = \frac{1}{2}(G_{slab}^i - N_{Si}^i g_{Mg_2SiO_4}^{slab}) - \Gamma_{Si,Mg}^i \mu_{Mg} - \Gamma_{Si,O}^i \mu_O \quad (7)$$

where parameters $\Gamma_{Si,Mg}^i$ and $\Gamma_{Si,O}^i$ are the excesses in the i terminated surface of Mg and O atoms with respect to the number of Si ions in the slab:

$$\Gamma_{Si,Mg}^i = \frac{1}{2}(N_{Mg}^i - N_{Si}^i \frac{N_{Mg}^{bulk}}{N_{Si}^{bulk}}) \quad (8)$$

To prevent the Mg, Si atoms and O_2 molecule from leaving the bulk of a Mg_2SiO_4 crystal and precipitating on the surface, their chemical potential must be less than the Gibbs free energy of the corresponding bulk²⁰:

$$\mu_{Mg} \leq g_{Mg}^{bulk} \quad (9)$$

$$\mu_{Si} \leq g_{Si}^{bulk} \quad (10)$$

Similarly, the precipitation of MgO and SiO_2 does not occur if

$$\mu_{Mg} + \mu_O \leq g_{MgO}^{bulk} \quad (11)$$

$$\mu_{Si} + 2\mu_O \leq g_{SiO_2}^{bulk} \quad (12)$$

Reuter and Scheffler²¹ have showed that the vibrational contribution to the surface Gibbs free energy is negligible in the case of RuO_2 (110) surfaces. However, the vibrational efface can be significant when surfaces with similar stabilities are compared. We explicitly introduce the vibrational part contribution into the Gibbs free energy. The Gibbs free energy g can be approximated as the total energy and F^{vib} :

$$g = E + F^{vib} - TS^{conf} + pV \approx E + F^{vib} \quad (13)$$

Here, the terms F^{vib} , T , p , V and S^{conf} correspond to the vibrational free energy, temperature, pressure, volume, and configurational entropy, respectively. In addition, the crystal volume per molecule is approximately 73.174 \AA^3 , so the largest pV term is only several meV for 100 atm pressure, which is negligible because of the DFT calculation errors. TS^{conf} is also approximated to be zero because of its negligible energetic contributions, as has been done in previous studies. Thus, g in Equation 13 is simplified to the contributions from only E and

F^{vib} . This F^{vib} term can be expressed using the phonon density of states (DOS) as follows:

$$F^{vib} = \frac{1}{2} \sum_{qj} \hbar \omega_{qj} + k_B T \sum_{qj} \ln[1 - \exp(-\hbar \omega_{qj}/k_B T)] \quad (14)$$

where q is the wave vector, j is the band index, and ω_{qj} is the phonon frequency of the phonon mode labeled by a set $\{q,j\}$. The phonon calculations were conducted based on the density functional perturbation theory (DFPT) implemented in VASP software in connection with the Phonopy software²².

By introducing the deviation of the Mg and Si chemical potentials, we have

$$\Delta\mu_{Mg} = \mu_{Mg} - g_{Mg}^{bulk} \quad (15)$$

and

$$\Delta\mu_{Si} = \mu_{Si} - g_{Si}^{bulk} \quad (16)$$

Then, we can rewrite Equation(5) as

$$2\Delta\mu_{Mg} + \Delta\mu_{Si} + 4\Delta\mu_O = \Delta g_f(Mg_2SiO_4) \quad (17)$$

where $\Delta g_f(Mg_2SiO_4)$ is the Gibbs free energy of formation for Mg_2SiO_4 from Mg, Si and O_2 in their standard states.

$$\Delta g_f(Mg_2SiO_4) = g_{Mg_2SiO_4}^{bulk} - 2g_{Mg}^{bulk} - g_{Si}^{bulk} - 2E_{O_2} \quad (18)$$

The above boundary conditions are transformed into:

$$\Delta\mu_{Mg} \leq 0 \quad (19)$$

$$2\Delta\mu_{Mg} + 4\Delta\mu_O \geq \Delta g_f(Mg_2SiO_4) \quad (20)$$

$$\Delta\mu_{Mg} + \Delta\mu_O \leq \Delta g_f(MgO) \quad (21)$$

$$\Delta\mu_{Mg} + \Delta\mu_O \geq \frac{1}{2}(\Delta g_f(Mg_2SiO_4) - \Delta g_f(SiO_2)) \quad (22)$$

$\Delta g_f(MgO)$ and $\Delta g_f(SiO_2)$ are the Gibbs free energies of formation for MgO and SiO_2 . The oxygen atoms in Mg_2SiO_4 are in equilibrium with oxygen gas in the atmosphere above the crystal surface:

$$\mu_O = \frac{1}{2}\mu_{O_2}^{gas} \quad (23)$$

Chemical potentials are difficult to access in experimental conditions. The oxygen gas chemical potential highly depends on the gas temperature and oxygen partial pressure. Therefore, this dependence helps us to express the Gibbs free energies for the Mg_2SiO_4 surface in terms of the temperature and oxygen gas partial pressure. We approximate the oxygen gas as an ideal gas, so

the dependence of the oxygen gas chemical potential on pressure can be written as

$$\begin{aligned}\mu_{O_2}^{gas}(T, P) &= \mu_{O_2}^{gas\ominus}(T) + kT \ln f_{O_2}(T, P) \\ &= \mu_{O_2}^{gas\ominus}(T) + kT \ln\left(\frac{P}{P^0}\right)\end{aligned}\quad (24)$$

where k is the Boltzmann constant. $\mu_{O_2}^{gas\ominus}(T)$ is the standard chemical potential of oxygen gas at temperature T , which we evaluated from the NIST-JANAF data²³. The variation of the oxygen atom chemical potential can be written as

$$\begin{aligned}\Delta\mu_O(T, P) &= \mu_O(T, P) - \frac{1}{2}E_{O_2} \\ &= \frac{1}{2}[\Delta G_{O_2}^{gas}(T, P^0) + kT \ln\left(\frac{P}{P^0}\right)] + \delta\mu_O^0\end{aligned}\quad (25)$$

$\Delta G_{O_2}^{gas}(T, P^0)$ is a change in oxygen gas Gibbs free energy at standard pressure P^0 and temperature T with respect to its Gibbs energy at 298.15 K. We present the calculated values for $\Delta G_{O_2}^{gas}(T, P^0)$ in Table III. $\delta\mu_O^0$ is a correction, which should match experimental data and results of the quantum-mechanical computations. This correction was estimated from the computation of metal oxides and metals similarly to the approach in Reuter and Scheffler²¹. In our calculation, $\delta\mu_O^0$ is 0.1997 eV and 0.4208 eV for SiO_2 and MgO , respectively. We use an average value of 0.3102 eV for the calculation hereafter.

Finally, we can write Equation 13 as

$$\Omega^i = \phi^i - \Gamma_{Si,Mg}^i \Delta\mu_{Mg} - \Gamma_{Si,O}^i \Delta\mu_O \quad (26)$$

ϕ^i is:

$$\begin{aligned}\phi^i &= \frac{1}{2}(G_{slab}^i - N_{Si}^i g_{Mg_2SiO_4}^{bulk}) - \Gamma_{Si,Mg}^i g_{Mg}^{bulk} - \frac{1}{2}\Gamma_{Si,O}^i E_{O_2} \\ &\approx \frac{1}{2}(E_{slab}^i + F_{slab}^{vib} - N_{Si}^i g_{Mg_2SiO_4}^{bulk}) \\ &\quad - \Gamma_{Si,Mg}^i g_{Mg}^{bulk} - \frac{1}{2}\Gamma_{Si,O}^i E_{O_2}\end{aligned}\quad (27)$$

We calculated the surface Gibbs free energies for all surfaces described in Section II A. The region where the Mg_2SiO_4 surface is stable with respect to the precipitation of Mg, Si or their oxides is determined using inequalities.

III. RESULTS AND DISCUSSION

A. Atomic and electronic structures

The optimized lattice constant of the bulk crystal obtained from our calculation is notably close to those

in previous studies from ab initio calculation^{9,24} and experiment²⁵ as shown in Table I.

After the relaxation of the slab surface, the top most atoms are dragged towards the bulk part and leave the ideal position in the crystal. The variation of the atom positions are listed in Table V. We use d_{rel} to evaluate the relative displacement of atoms after the relaxation.

$$d_{rel} = \frac{\Delta Z_{i,j}^{origin} - \Delta Z_{i,j}^{relaxed}}{\Delta Z_0} \quad (28)$$

where $\Delta Z_{i,j}^{origin}$ is the distance between atoms i and j in the unrelaxed slabs; $\Delta Z_{i,j}^{relaxed}$ is the distance between atoms i and j in the relaxed surface slab; and ΔZ_0 is the length of the unit cell of the forsterite crystal. For d_{rel} , a positive sign implies a contraction between the surface layers, whereas a negative sign implies an expansion. We used slab models thicker than 2 times of the bulk crystal (more than 40 layers), and the relative displacement quickly converged in several layers of atoms. Figure 6 shows that the displacement rapidly decreases to the vicinity of 0 in fewer than 10 layers. At the same time, a unit cell of bulk crystal forsterite has 19 layers in the [010] direction. In M1, O2 and O2-II terminations, the topmost two layers have the identical type of atom. These atoms remain in the same layer after relaxation. In almost all terminations, the displacement between O and Mg atoms is larger than the displacement between O and Si or O layers. For example, in the M1 and M2 terminations, the Mg atoms in the topmost layers are heavily dragged towards the bulk to form a large positive d_{rel} . The O atom in the topmost layer of the O and O-II termination seams is less constrained. An interlayer expansion appears in the first two layers of these two terminations. Si and O are also split into two layers at the topmost SiO and SiO-II terminations.

The calculated Bader charges for different atoms of the outermost few layers of all nine terminations are shown in Table VI. For reference, the charges of Mg, Si, and O atoms in the bulk Mg_2SiO_4 are also listed in Table VI. Compared to the electronic charges of atoms in bulk Mg_2SiO_4 , the corresponding charges of the atoms in the outermost few layers become closer with the increase in surface layer number. The M2, O-II and SiO-II terminations have the obviously smaller charge difference among these nine terminations. The variations are all not larger than 0.05 e in the first 10 layers, as shown in the Table. VI. Other six terminations have similar charge variations of approximately 1.50 e in the first 10 layers.

B. Cleavage energy

The energies required to create complementary surface pairs for forsterite (010) were calculated using Equations (1) and (2), and the results are collected in Table II. The largest cleavage energy was obtained for a pair of

O2- and SiO-terminated (010) surfaces. The lowest energy is the creation of an M2-M2 terminated (010) surface pair. This slab is also the only stoichiometric slab. Therefore, one should expect the formation of these surfaces, when an Mg_2SiO_4 crystal is cleaved perpendicular to the [010] direction. Thus, the M2 termination is the most popular termination in previous forsterite surface-related studies.^{10,26,27} Hence, a more realistic expectation is that an attempt to cleave Mg_2SiO_4 perpendicular to the [010] direction will lead to saw-shaped surface formation. The following evolution of these surfaces depends on possibilities of ion exchange between crystal bulk and surface, surface and environment, and mobility of atoms on the surface.

C. Surface stability with different terminations

The cleavage energy measures the energy to split a crystal into two parts with complementary terminations. Therefore, the cleavage energy cannot be used to study the stability of different surfaces in various chemical conditions. The Gibbs surface free energy is a measure of the excess energy of a semi-infinite crystal in contact with matter reservoirs, which can be used to analyse the stability of surface slabs. The *ab initio* simulation enabled us to determine all parameters needed to calculate surface free energies for a variety of surfaces and formation energies for Mg_2SiO_4 , MgO and SiO_2 crystals. The excess of oxygen and Mg atoms with respect to Si atoms in the simulated slabs and values are calculated and listed in Table IV. A spontaneous surface formation line of every surface with a specific termination, which are presented on phase diagrams show on the left part of Fig. 7 with a label of the termination name, can be determined by solution of equation

$$\Omega^i(\Delta\mu_{Mg}, \Delta\mu_O) = 0 \quad (29)$$

The direction indicated by the arrow on each spontaneous formation line, i.e., the Gibbs free energies become positive, which suggests that these examined terminations are stable and may be exposed over the Mg_2SiO_4 particles under the given conditions. The most stable surface for any particular value of the Mg and O chemical potentials is the surface with the smallest surface Gibbs free energy value and with a positive Gibbs free energy. The boundaries among the regions of stability for different terminations are marked by red dashed lines. The boundary between stability regions for surfaces with terminations *i* and *j* is determined by solution of the equation.

$$\Omega^i(\Delta\mu_{Mg}, \Delta\mu_O) = \Omega^j(\Delta\mu_{Mg}, \Delta\mu_O) \quad (30)$$

In the present study, only three surface terminations satisfy the two conditions at the same time. Thus, we

only plot two boundaries of these three surfaces. On the left part of Fig. 7, each colour block represents the region of stability for different surface terminations.

Pure Mg_2SiO_4 exists when the conditions of Equations (19) - (22) are all satisfied. All of these conditions are shown in Fig. 7 as solid lines. The formation energies of Mg_2SiO_4 , magnesium and silicon oxides determine the position of respective precipitation lines. Precipitation of silicon occurs below the Si precipitation line, magnesium metal precipitates on the right from the magnesium precipitation line. MgO crystal will grow on the right and above the MgO precipitation line, and SiO_2 will grow on the left from the SiO_2 precipitation line. A pure Mg_2SiO_4 can only be obtained in the narrow striped region between the MgO precipitation line on the left and the SiO_2 precipitation line on the right. At the bottom of the diagram, the strip is limited by the Si precipitation line.

The calculated stability diagram is presented in Fig. 7. It shows the regions of oxygen and magnesium chemical potentials, where the surface free energies [Equation (26)] that are calculated for different terminations are minimal. Every colour block is a stability zone of the relative surface slab.

At each point on the diagram, the Mg_2SiO_4 surface is in equilibrium with oxygen gas. The equilibrium is characterized by the oxygen chemical potential. Since a single value for the chemical potential can correspond to a wide spectrum of various temperatures and pressures, we draw dependencies of the oxygen chemical potentials on temperature for a number of gas pressures on the right side of Fig. 7. These functions were calculated from experimental data, taken from the thermodynamical tables²³ following the approach described earlier by Equation (25). The design used for building diagrams in Fig. 7 enables us to determine the conditions for the oxygen environment, which correlate with the points on the phase diagrams on the left side of the figures.

To illustrate the behaviour of surface Gibbs free energies for different Mg_2SiO_4 surfaces, we have plotted the Gibbs free energies for several specific conditions. The surface Gibbs free energies defined in Eq. 26 for an oxygen gas pressure equal to 1 bar are plotted in Fig. 8 and Fig. 9 and represent the ambient condition and near-melting condition²⁸, respectively. At smaller $\Delta\mu_{Mg}$ (corresponding to Mg-poor conditions), the most stable surface is SiO-II terminated. Under the condition for the toward the Mg-rich environment, the M2, O-II terminated surfaces become stable. In both high- and low-temperature conditions, the relative stability order of these surface terminations is maintained.

IV. CONCLUSION

We used DFT calculations and thermodynamic methods to analyse nine possible surface terminations of forsterite (010) surfaces. We analysed the dependence of

their relative stabilities versus the magnesium and oxygen chemical potentials.

Because the cleavage energy to create a pair of M2 terminated surfaces is much smaller than the cleavage energy to create other pairs of surfaces, when a forsterite crystal is cleaved perpendicular to the [010] direction, it will be highly possible to observe an M2 terminated surface. The cleavage energy of creating an O-II + SiO-II pair is slightly larger than that for the M2-M2 pair.

The comparison of the surface Gibbs free energies for different surface terminations shows that among the potential (010) surfaces, a stability diagram has been obtained in this study. In the Mg-poor condition, SiO-II have the smallest surface Gibbs free energy. When the condition becomes Mg-rich, the most stable termination will be M2 and O-II. We analysed different projections of the phase diagram under the ambient condition and high-temperature condition. The stability order does not

change with the increase in temperature.

Our simulations provide a foundation for further theoretical studies of forsterite surfaces, particularly the studies of non-stoichiometric surfaces, possible surface reconstructions, and chemical processes on forsterite surfaces.

V. ACKNOWLEDGEMENTS

This work was supported by National Science Foundation of China (Grants #41503060 and #41590620), Strategic Priority Research Program (B) of Chinese Academy of Sciences (# XDB18000000 and # XDB10020301). Dr. Javed Hussain is thanked for providing help in VASP calculation and useful discussion in early stage of this research. Computations were performed on resources provided by the Computer Simulation Lab, IGGCAS and High-Performance Computing in University of Iceland.

-
- * gengming@mail.iggcas.ac.cn
† hj@hi.is
- ¹ M. Stimpfl, A. M. Walker, M. J. Drake, N. H. de Leeuw, and P. Deymier, *Journal of Crystal Growth* **294**, 83 (2006).
 - ² N. H. de Leeuw, C. R. A. Catlow, H. E. King, A. Putnis, K. Muralidharan, P. Deymier, M. Stimpfl, and M. J. Drake, *Chemical Communications* **46**, 8923 (2010).
 - ³ K. Muralidharan, P. Deymier, M. Stimpfl, N. H. de Leeuw, and M. J. Drake, *Icarus* **198**, 400 (2008).
 - ⁴ H. E. King, M. Stimpfl, P. Deymier, M. J. Drake, C. R. A. Catlow, A. Putnis, and N. H. de Leeuw, *Earth and Planetary Science Letters* **300**, 11 (2010).
 - ⁵ R. Trias, B. Mnez, P. le Campion, Y. Zivanovic, L. Lecourt, A. Lecoeuvre, P. Schmitt-Kopplin, J. Uhl, S. R. Gislason, H. A. Alfresson, K. G. Mesfin, S. . Subjrnstttr, E. S. Aradttir, I. Gunnarsson, J. M. Matter, M. Stute, E. H. Oelkers, and E. Grard, *Nature Communications* **8**, 1063 (2017).
 - ⁶ G. W. Watson, P. M. Oliver, and S. C. Parker, *Physics and Chemistry of Minerals* **25**, 70 (1997).
 - ⁷ N. H. de Leeuw, S. C. Parker, C. R. A. Catlow, and G. D. Price, *American Mineralogist* **85**, 1143 (2000).
 - ⁸ N. H. de Leeuw, *The Journal of Physical Chemistry B* **105**, 9747 (2001).
 - ⁹ M. Bruno, F. R. Massaro, M. Prencipe, R. Demichelis, M. De La Pierre, and F. Nestola, *The Journal of Physical Chemistry C* **118**, 2498 (2014).
 - ¹⁰ S. Garcia-Gil, D. Teillet-Billy, N. Rougeau, and V. Sidis, *The Journal of Physical Chemistry C* **117**, 12612 (2013).
 - ¹¹ R. Demichelis, M. Bruno, F. R. Massaro, M. Prencipe, M. De La Pierre, and F. Nestola, *Journal of Computational Chemistry* **36**, 1439 (2015).
 - ¹² A. M. Asaduzzaman, S. Laref, P. A. Deymier, K. Runge, H.-P. Cheng, K. Muralidharan, and M. J. Drake, *Philosophical Transactions of the Royal Society A: Mathematical, Physical and Engineering Sciences* **371** (2013), 10.1098/rsta.2011.0582.
 - ¹³ H. Yan, C. Park, G. Ahn, S. Hong, D. T. Keane, C. Kenney-Benson, P. Chow, Y. Xiao, and G. Shen, *Geochimica et Cosmochimica Acta* **145**, 268 (2014).
 - ¹⁴ G. Kresse and J. Hafner, *Physical Review B* **47**, 558 (1993).
 - ¹⁵ G. Kresse and J. Hafner, *Physical Review B* **49**, 14251 (1994).
 - ¹⁶ G. Kresse and J. Furthmüller, *Computational Materials Science* **6**, 15 (1996).
 - ¹⁷ G. Kresse and J. Furthmüller, *Physical Review B* **54**, 11169 (1996).
 - ¹⁸ P. E. Blchl, *Physical Review B* **50**, 17953 (1994).
 - ¹⁹ J. P. Perdew, K. Burke, and M. Ernzerhof, *Physical Review Letters* **77**, 3865 (1996).
 - ²⁰ G. W. Watson, E. T. Kelsey, N. H. de Leeuw, D. J. Harris, and S. C. Parker, *Journal of the Chemical Society, Faraday Transactions* **92**, 433 (1996).
 - ²¹ K. Reuter and M. Scheffler, *Physical Review B* **65**, 035406 (2001).
 - ²² A. Togo and I. Tanaka, *Scripta Materialia* **108**, 1 (2015).
 - ²³ M. W. Chase, *NIST-JANAF Thermochemical Tables, 4th Edition* (American Institute of Physics, 1998).
 - ²⁴ M. S. Jos, A. Emilio, D. G. Julian, G. Alberto, J. Javier, O. Pablo, and S.-P. Daniel, *Journal of Physics: Condensed Matter* **14**, 2745 (2002).
 - ²⁵ A. Kirfel, T. Lippmann, P. Blaha, K. Schwarz, D. F. Cox, K. M. Rosso, and G. V. Gibbs, *Physics and Chemistry of Minerals* **32**, 301 (2005).
 - ²⁶ S. Kerisit, J. H. Weare, and A. R. Felmy, *Geochimica et Cosmochimica Acta* **84**, 137 (2012).
 - ²⁷ J. Navarro-Ruiz, P. Ugliengo, A. Rimola, and M. Sodupe, *The Journal of Physical Chemistry A* **118**, 5866 (2014).
 - ²⁸ B. T. C. Davis and J. L. England, *Journal of Geophysical Research* **69**, 1113 (1964).

TABLE I. Experimental and Calculated Values for Cell Parameters of Bulk Forsterite (in Å)

Lattice Constant	This work	Experiment ²⁵	Gaussian Basis ²⁴	Bruno et al. ⁹
a	4.7654	4.756	4.804	4.7892
b	10.2396	10.207	10.280	10.2539
c	5.9984	5.980	6.032	6.0092

TABLE II. Calculated Cleavage Energies

Created pairs of surfaces	Cleavage energy (eV/unit cell)	Cleavage energy (J/m ²)
M1 + O	11.765	6.594
M2 + M2	3.619	2.029
M2-II + O2-II	9.841	5.516
O-II + SiO-II	5.586	3.130
O2 + SiO	11.904	6.672

TABLE III. Variation in Gibbs free energy for oxygen gas at standard pressure with respect to its value at 0 K. Data are taken from NIST-JANAF table²³

T(K)	$\Delta G_{O_2}^{gas}(T, p^0)(eV)$	$\Delta G_O^{gas}(T, p^0)(eV)$	T(K)	$\Delta G_{O_2}^{gas}(T, p^0)(eV)$	$\Delta G_O^{gas}(T, p^0)(eV)$
100	-0.146	-0.073	800	-1.699	-0.850
200	-0.338	-0.169	900	-1.945	-0.973
298.15	-0.539	-0.270	1000	-2.196	-1.098
300	-0.545	-0.273	1100	-2.450	-1.225
400	-0.762	-0.381	1200	-2.708	-1.354
500	-0.987	-0.495	1300	-2.968	-1.493
600	-1.219	-0.610	1400	-3.232	-1.616
700	-1.457	-0.729	1500	-3.498	-1.749

TABLE IV. Excesses of O and Mg atoms in slabs with respect to Si atoms and the free energy of formation for various surfaces

Surface i	N_{Si}	$\Gamma_{Si, Mg}^i$	$\Gamma_{Si, O}^i$	$\phi^i(eV/unitcell)$	$\phi^i(J/m^2)$
M1-term.	8	1	0	2.645	1.483
M2-term	8	0	0	1.810	1.014
M2-II-term	8	1	0	2.163	1.212
O-term	10	-1	0	9.154	5.131
O-II-term	8	1	1	-3.057	-1.713
O2-term	8	1	2	-0.839	-0.469
O2-II-term	10	-1	0	9.878	5.537
SiO-term	10	-1	-2	12.815	7.186
SiO-II-term	10	-1	-1	8.642	4.844

TABLE V. Atom displacement of the topmost layers of nine terminated surfaces ($d_{rel}(\%)$)

M1 term.	M2 term.	M2-II term.	O term.	O-II term.	O2 term.	O2-II term.	SiO term.
4.45 (M1-O1)	4.64 (M2-O2)	-1.44 (M2-M2)	-8.73 (O1-SiO)	-1.75 (O1-M1)	0.70 (O2-M2)	-0.12 (O2 split)	-3.09 (SiO split)
-1.53 (O1-SiO)	0.22 (O2-SiO)	0.94 (M2-O2)	4.15 (SiO-O2)	3.84 (M1-O1)	1.15 (M2-M2)	-1.99 (O2-SiO)	0.47 (Si-O1)
-1.35 (SiO split)	-1.51 (SiO split)	-0.36 (O2 split)	-5.17 (O2 split)	-1.42 (O1-SiO)	-0.12 (M2-O2)	-1.57 (SiO split)	-0.32 (O1-M1)
-1.73 (SiO-O2)	0.16 (SiO-O1)	0.03 (O2-SiO)	1.89 (O2-M2)	-0.23 (SiO split)	-0.13 (O2 split)	-0.11 (SiO-O1)	2.76 (M1-O1)
1.20 (O2-M2)	0.74 (O1-M1)	-0.54 (SiO split)	-0.48 (M2-M2)	-0.66 (SiO-O2)	-0.25 (O2-SiO)	1.55 (O1-M1)	-1.75 (O1-SiO)
-2.09 (M2-M2)	0.36 (M1-O1)	-1.16 (SiO-O1)	-0.61 (M2-O2)	1.42 (O2-M2)	-0.72 (SiO split)	-0.13 (M1 split)	-0.22 (SiO split)
0.88 (M2-O2)	-0.16 (O1-SiO)	1.32 (O1-M1)	-1.60 (O2 split)	-2.27 (M2-M2)	0.04 (SiO-O1)	-1.20 (M1-O1)	-0.68 (SiO-O2)
-0.05 (O2-SiO)	-0.99 (SiO split)	-1.67 (M1 split)	-0.65 (O2-SiO)	0.75 (M2-O2)	0.27 (O1-M1)	0.29 (O1-SiO)	0.70 (O2-M2)
-0.41 (SiO-O1)	0.13 (SiO-O2)	1.51 (M1-O1)	-0.71 (SiO-O1)	-0.51 (O2-SiO)	0.34 (M1-O1)	-0.43 (SiO split)	-0.51 (M2-M2)
0.35 (O1-M1)	0.62 (O2-M2)	-0.58 (O1-SiO)	0.65 (O1-M1)	-0.40 (SiO split)	-0.53 (O1-SiO)	-0.21 (SiO-O2)	0.30 (M2-O2)

TABLE VI. Bader charges of the bulk crystal and slab with different terminations

Unit Cell		M1 term.		M2 term.		M2-II term.		O term.		O-II term.		O2 term.		O2-II term.		S
atom	charge	atom	charge	atom	charge	atom	charge	atom	charge	atom	charge	atom	charge	atom	charge	at
Mg(M1)	1.67	Mg(M1)	1.59	Mg(M2)	1.66	Mg(M2)	0.44	O(O1)	-0.72	O(O1)	-1.60	O(O2)	-0.86	O(O2)	-1.06	Si(S
Mg(M2)	1.69	O(O1)	-1.60	O(O2)	-1.60	Mg(M2)	1.45	O(SiO)	-0.89	Mg(M1)	1.64	O(O2)	-0.88	O(O2)	-1.07	O(S
O(O1)	-1.63	O(SiO)	-1.62	Si(SiO)	3.09	O(O2)	-1.63	Si(SiO)	3.08	O(O1)	-1.59	Mg(M2)	1.67	O(SiO)	-1.49	O(
O(O2)	-1.61	Si(SiO)	1.62	O(SiO)	-1.58	O(O2)	-1.70	O(O2)	-1.56	O(SiO)	-1.62	Mg(M2)	1.68	Si(SiO)	3.07	Mg
O(SiO)	-1.62	O(O2)	-1.61	O(O1)	-1.62	O(SiO)	-1.66	O(O2)	-1.58	Si(SiO)	3.08	O(O2)	-1.58	O(O1)	-1.35	O(
Si(SiO)	3.1	Mg(M2)	1.68	Mg(M1)	1.66	Si(SiO)	3.09	Mg(M2)	1.68	O(O2)	-1.61	Si(SiO)	3.08	Mg(M1)	1.67	O(S
		Mg(M2)	1.68	O(O1)	-1.61	O(O1)	-1.64	O(O2)	-1.59	Mg(M2)	1.69	O(SiO)	-1.60	O(O1)	-1.55	Si(S
		O(O2)	-1.61	O(SiO)	-1.61	Mg(M1)	1.66	O(O2)	-1.62	Mg(M2)	1.68	O(O1)	-1.61	O(SiO)	-1.59	O(
		Si(SiO)	3.08	Si(SiO)	3.08	O(O1)	-1.62	Si(SiO)	3.10	O(O2)	-1.60	Mg(M1)	1.66	Si(SiO)	3.08	Mg
		O(SiO)	-1.60	O(O2)	-1.60	O(SiO)	-1.60	O(SiO)	-1.62	O(SiO)	-1.59	O(O1)	-1.61	O(O2)	-1.54	O(

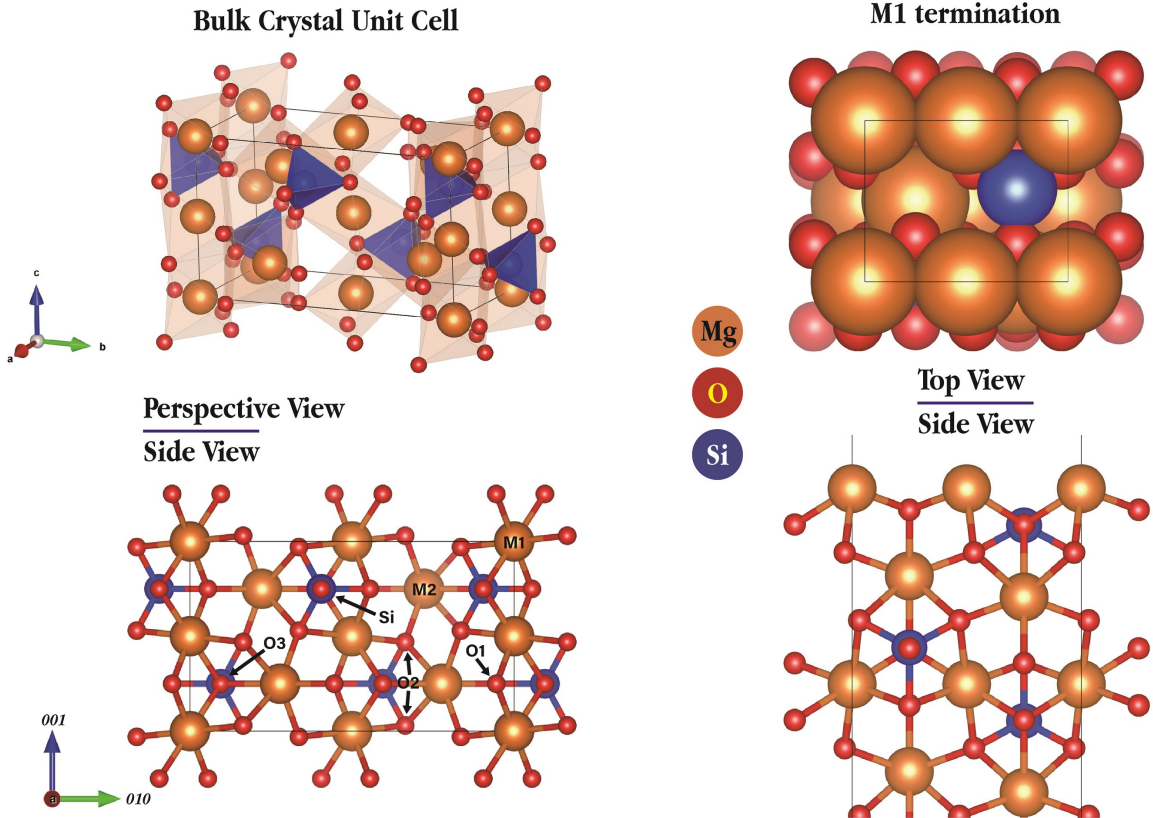


FIG. 1. Structure of the forsterite unit cell and M1 termination

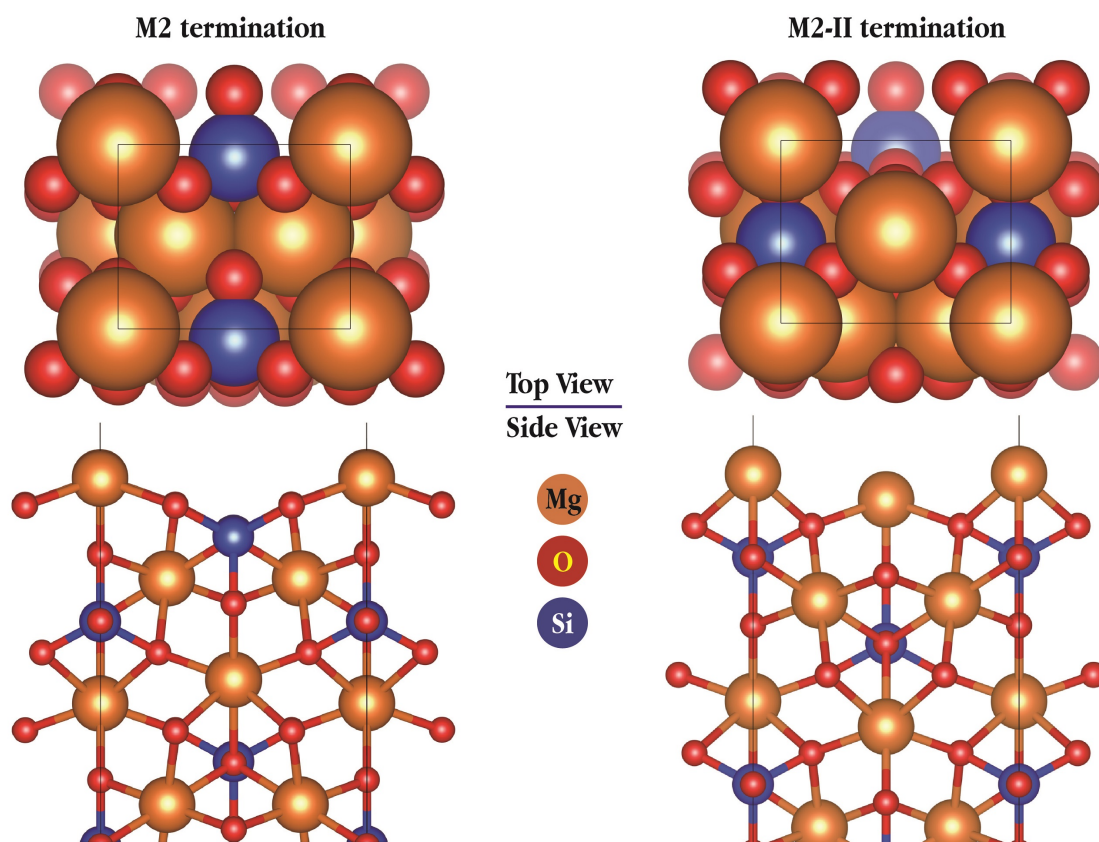


FIG. 2. M2 termination surface structure

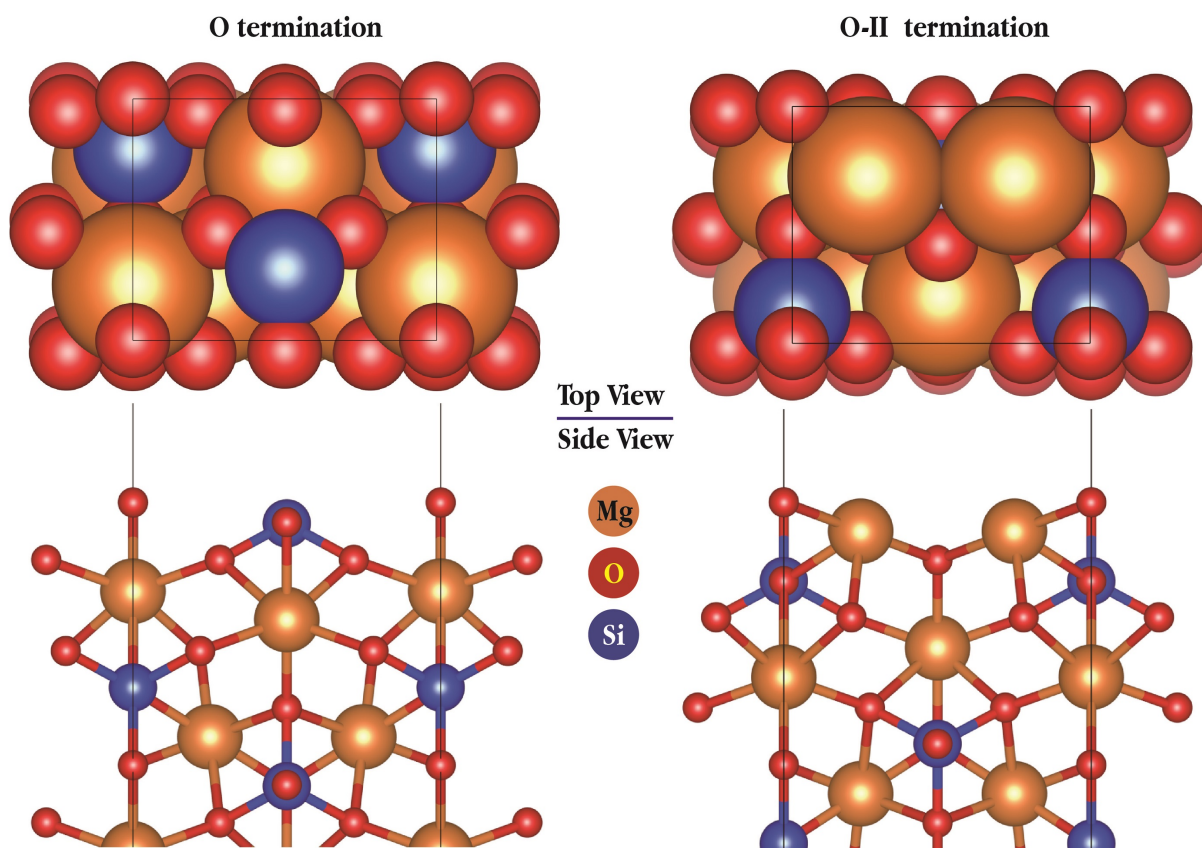


FIG. 3. O termination surface structure

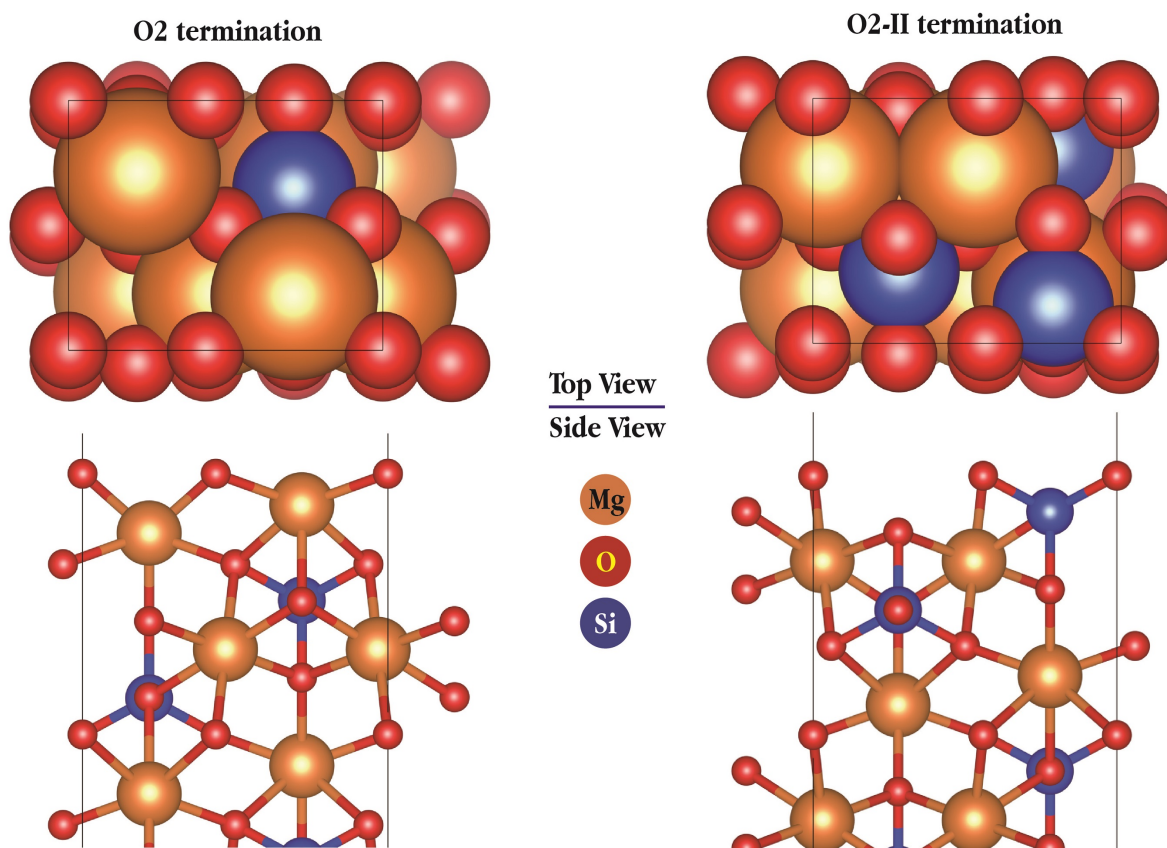


FIG. 4. O2 termination at the surface structure

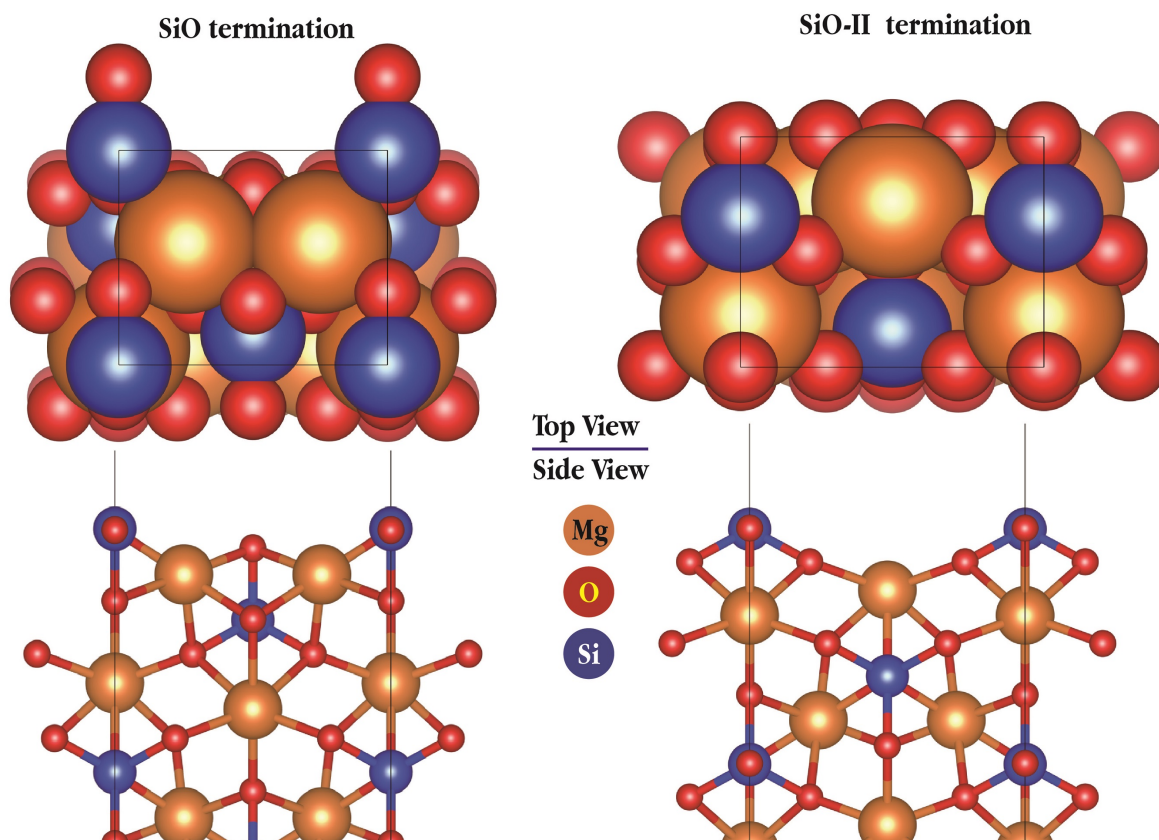


FIG. 5. SiO termination at the surface structure

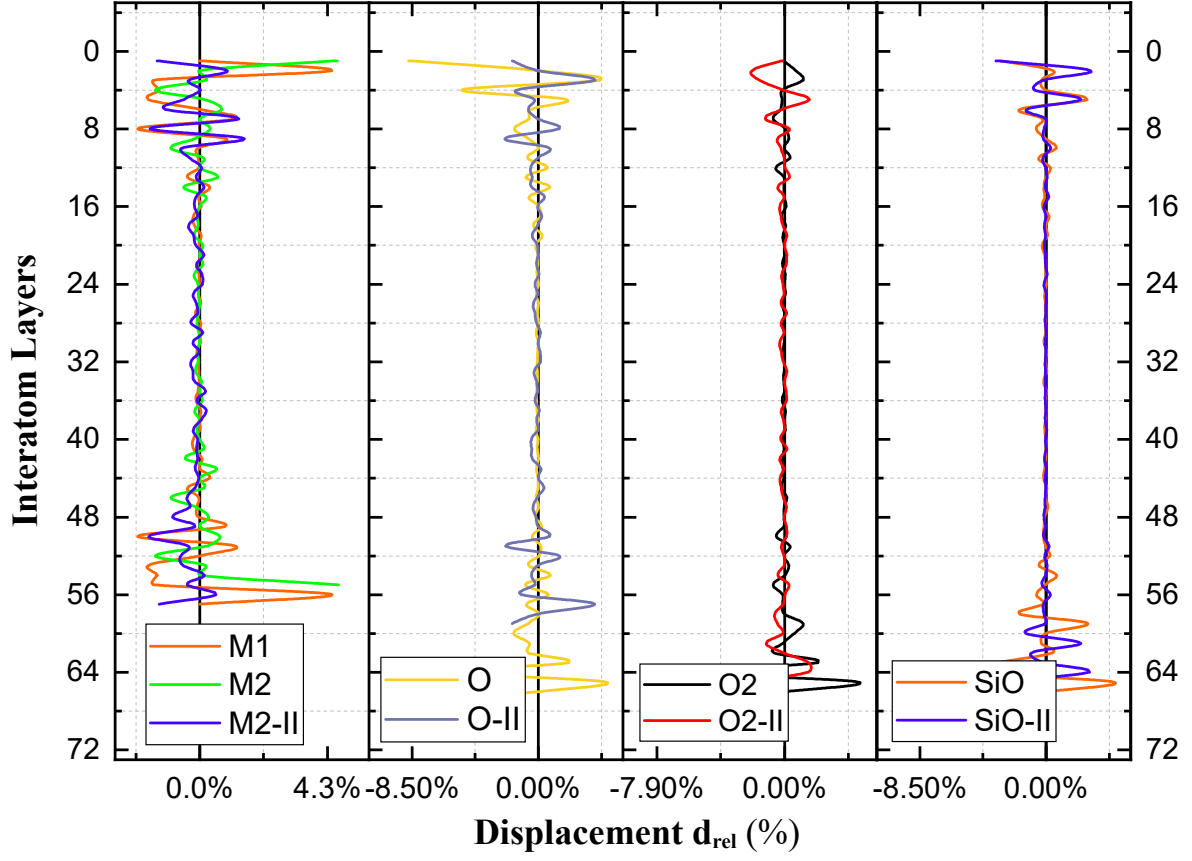


FIG. 6. Displacement oscillation pattern of the relaxed atom layers

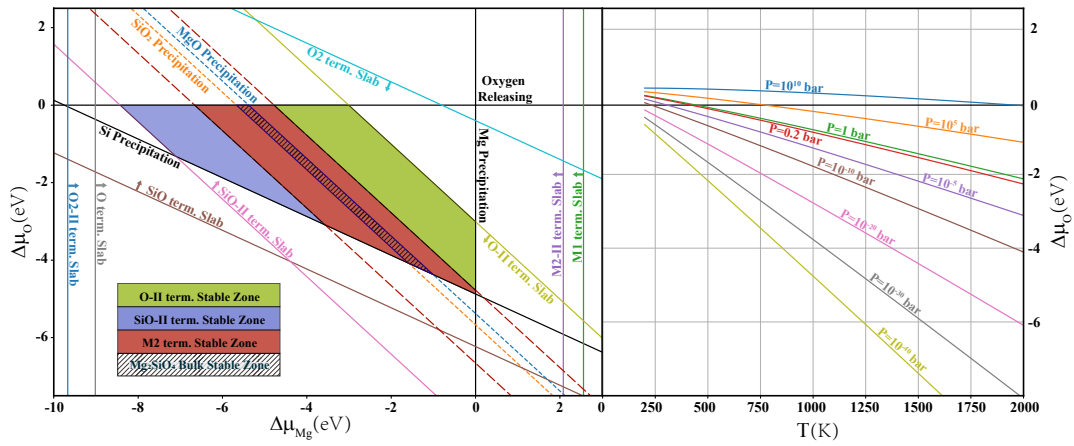


FIG. 7. Phase diagram: the regions of stability of the Mg_2SiO_4 (010) surfaces with different terminations as functions of the chemical potential variations for Mg and O atoms

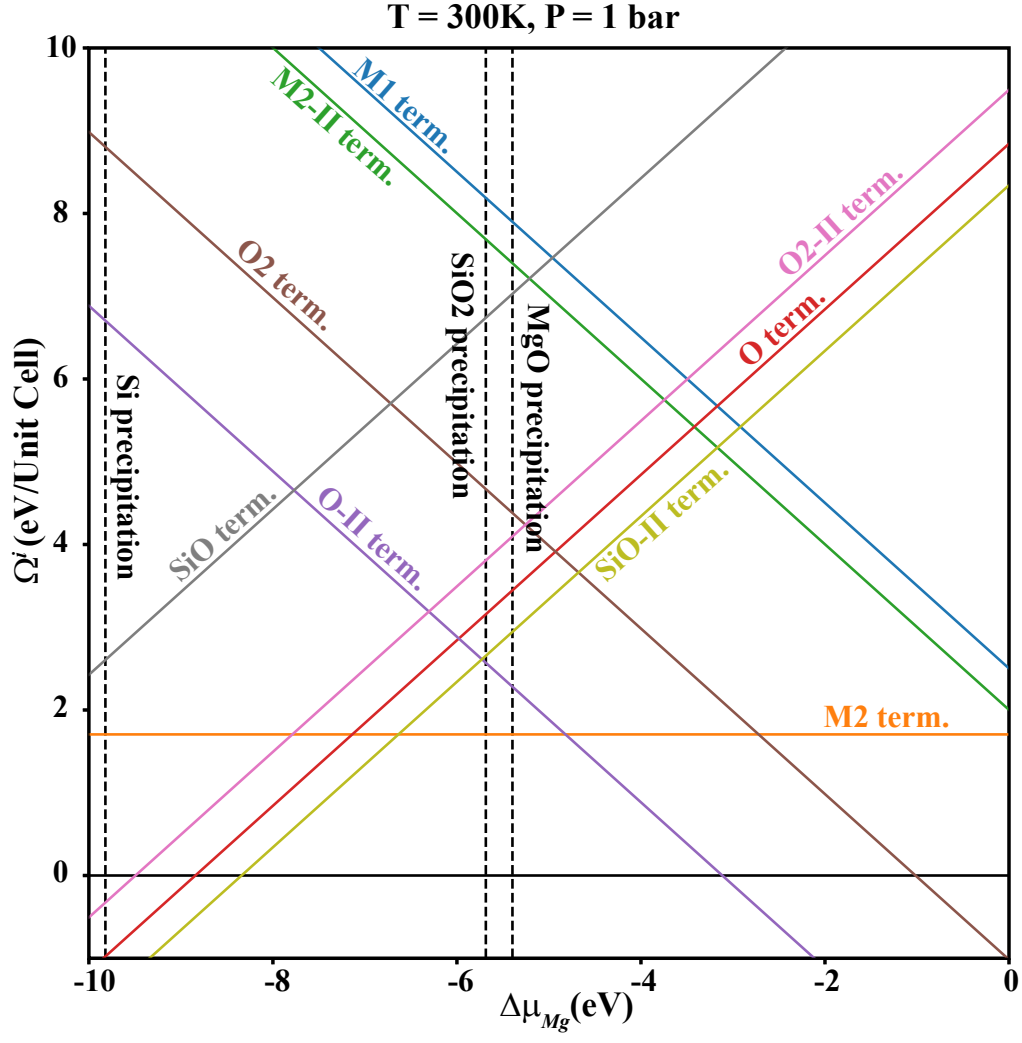


FIG. 8. Surface Gibbs free energy as a function of $\Delta\mu_{Mg}$ at $T=300\text{ K}$ and $p_{O_2} = 1\text{ bar}$

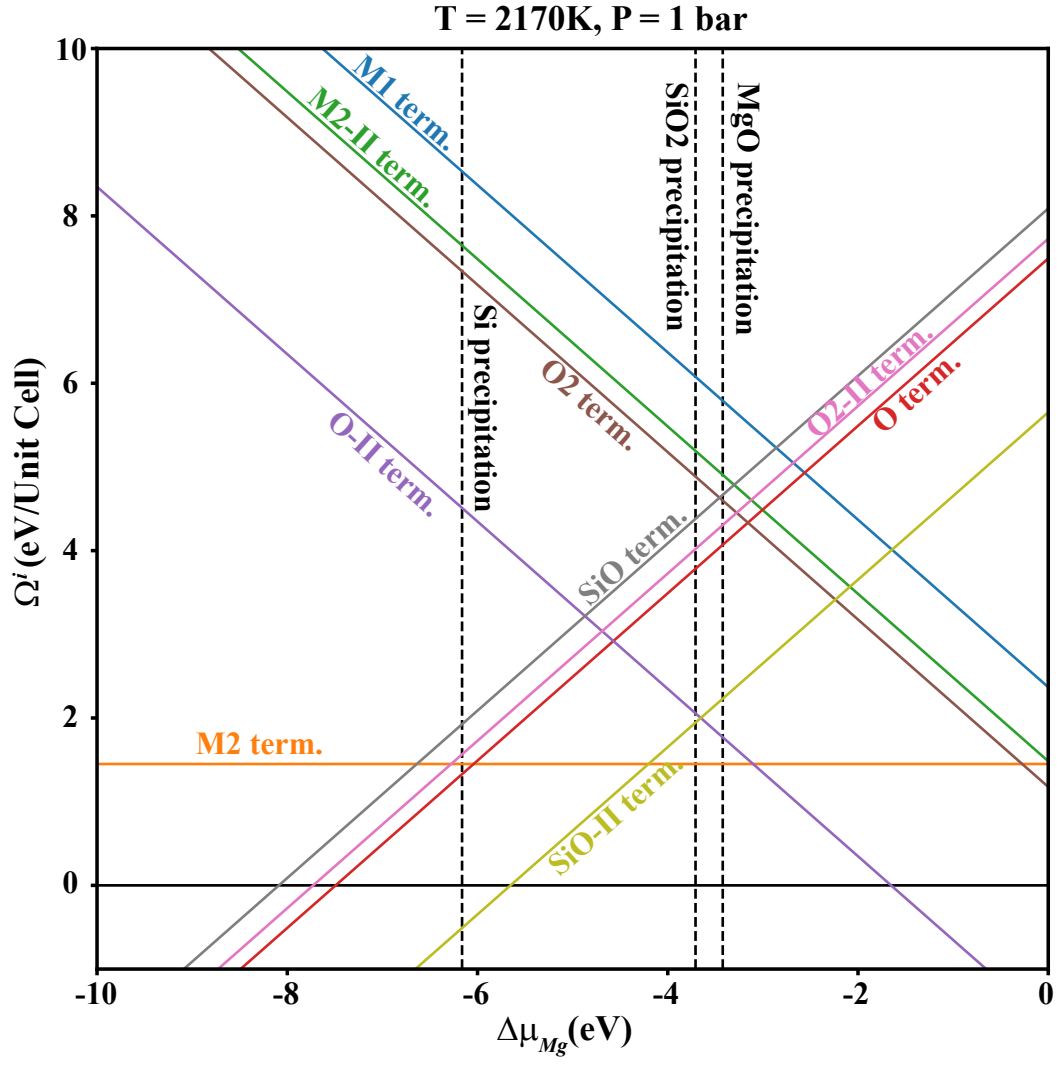


FIG. 9. Surface Gibbs free energy as a function of $\Delta\mu_{Mg}$ at $T=2170\text{ K}$ and $p_{O_2} = 1\text{ bar}$